This is the Pre-Published Version.

Ethylene and power cogeneration from proton ceramic fuel cells (PCFC): a thermo-electrochemical modelling study

Zheng Li, Qijiao He, Chen Wang, Qidong Xu, Guo Meiting, Idris Temitope Bello, Meng Ni*

Department of Building and Real Estate, Research Institute for Sustainable Urban Development (RISUD) & Research Institute for Smart Energy (RISE), The Hong Kong Polytechnic University, Hung Hom, Kowloon, Hong Kong, China

* Corresponding author: Meng Ni
Email: meng.ni@polyu.edu.hk; Tel: 852-27664152

Abstract

Ethylene is a vital chemical worldwide but its production is very energy-intensive with high CO_2 emissions. C_2H_6-fueled proton ceramic fuel cells (PCFCs) are promising electrochemical processes for cogeneration of ethylene and electric power with high performance and low emission. Herein, a tubular thermos-electrochemical model is established to investigate the characteristics of C_2H_6-fueled PCFC. Parametric studies are performed to examine the effects of operating voltage, inlet fuel flow rate, and inlet temperature on PCFC cogeneration performance. PCFC under open-circuit voltage (OCV) condition at 700 °C, the ethane conversion and ethylene selectivity are 15.69% and 99.47%, respectively. The ethylene production is enhanced by the electrochemical reaction. At 0.4V and 700°C, the conversion of ethane is increased to 32.59% and the PCFC can deliver a peak power density of 146.12mW cm^{-2}. Increasing the inlet temperature significantly improves the cogeneration performance of PCFC but also increases the temperature gradient in the cell. In addition, H_2 depletion in the anode results in local electrochemical performance degradation. The results demonstrate the enhanced ethylene production by electrochemical processes and the operating and structural parameters can be optimized in the subsequent study to further improve ethylene production.

Keywords

Nomenclature

Abbreviation

PCFC	Proton ceramic fuel cell
OCV	Open circuit voltage
EDH	Ethane dehydrogenation
IRA	Internal reforming area
ERA	Electrochemical reaction area
PPD	Peak power density
MF	Methane formation
TPB	Triple phase boundary
DOF	Degrees of freedom
EH	Electrolyte heat source
CH	Carhodew heat source
ACH	Anode channel heat source
AH	Anode heat source
CNH	Cell net heat source
OH	Ohmic heat source
HER	Hydrogen electrochemical reaction heat source
ChemR	Chemical reaction heat source
ANH	Anode side net heat source

Letter

E_{eq}	Equilibrium potential, V
R	Universal molar gas constant, 8.314 J mol^{-1} k^{-1}
T	Working temperature, K
F	Faraday constant, 96485.33 C mol^{-1}
P_i^l	Partial pressure of species of i, Pa
i	Current density, A m^{-2}
$E_{act,i}$	Activation energy for the chemical/electrochemical reaction of species i, J
ΔH_f^O	Standard formation entropy, J mol^{-1}

Symbol	Description
R_i	Reaction rate of species i, mol m^{-3} s^{-1}
y_i	Molar fraction of species i, mol s^{-1}
K_{eq}	Reaction rate equilibrium constant
k_r^0	Pre-exponential factor for each rate constant
V_i	Volume fraction of phase i
l_{TPB}	TPB length, m^2 m^{-3}
M_i	Molar mass of species i, kg mol^{-1}
$\boldsymbol{u}$	Velocity, m s^{-1}
$\boldsymbol{N}_i$	Molar flux of species I, mol m^{-2} s^{-1}
D_{iK}^{eff}	Effective Knudsen diffusion coefficient of species i, m^2 s^{-1}
D_{ij}^{eff}	Effective binary diffusion coefficient, m^2 s^{-1}
T_b	Boiling temperature at the standard air pressure, K
C_p	Thermal capacity, J mol^{-1} k^{-1}
k	Thermal conductivity, W m^{-1} k^{-1}
ΔS	Entropy change of reaction, J K^{-1} mol^{-1}
Q_i	Source term i
$x_{an/ca,inlet}$	Inlet composition at the anode/cathode side gas channel, %
$X_{C_2H_6}$	Ethane conversion, %
$S_{C_2H_4}$	Ethylene selectivity, %
$v_{an/ca,inlet}$	Inlet volumetric flow rate at the anode/cathode side gas channel, SCCM
ρ	Density, kg m^{-3}
σ_i	Conductivity of phases i, S m^{-1}
ε	Porosity
τ	Tortuosity
k	Permeability, m^2
ω_i	Mass fraction of species i
μ	Viscosity, Pa s
φ_{ij}	Inter-collisional parameter
Ω_D	Temperature-dependent collision integral

1
2
3
4
5
6
7
8
9
10
11
12
13
14
15
16
17
18
19
20
21
22
23
24
25
26
27
28
29
30
31
32
33
34
35
36
37
38
39
40
41
42
43
44
45
46
47
48
49
50
51
52
53
54
55
56
57
58
59
60
61
62
63
64
65

1. Introduction

Ethylene is widely considered as the building block in the petrochemical industry. Worldwide ethylene production has grown substantially in recent years. For example, from 2005 to 2016, the average annual growth rate of ethylene production in China is 8.1% [1]. Meanwhile, the U.S. shale gas revolution led to a considerable increase in ethylene capacity [2]. At present, the wave of construction of ethylene production units has swept the world. Both the U.S. and China have announced plans to boost ethylene production, involving tens of billions of dollars in investment [3,4]. Currently, the conventional approach to producing ethylene is the steam cracking process of easy-accessible hydrocarbons, mainly ethane and naphtha [5]. More than 140 megatons of ethylene are produced globally through steam cracking processes per year [6]. Nonetheless, the steam cracking process has several drawbacks. On the one hand, it is an energy-intensive process (working temperature can be up to 1000 °C) owing to the endothermic cracking reaction and is limited by thermodynamics. On the other hand, the process requires periodic shutdowns to burn out coke [4]. Ethylene production demands 16 GJ/ton of heat energy and emits nearly 1.2 tons of CO_2 [2]. Based on the above discussion, developing an efficient approach for ethylene production with low CO_2 emission can be a new driving force for improving ethylene production capacity and sustainability. In addition, regarding current climate change and energy shortage, the new approach should have economic and environmental attractiveness.

The electrochemical method has a great potential to be a substitute. PCFCs are efficient devices to convert chemical energy into electrical power [7,8]. Recently, the production of ethylene using PCFC has attracted increasing research attention [9]. Specifically, ethane is fed to the anode of the PCFC for ethane dehydrogenation (EDH) to produce ethylene and hydrogen [10]. Meanwhile, hydrogen is electrochemically consumed to generate protons and electrons. The consumption of hydrogen can favour the EDH reaction. The heat released from electrochemical

5

reactions can also be a heat source for the endothermic reaction. Therefore, PCFC can overcome the drawbacks of the conventional thermal cracking process. Besides, the electrons can be collected for electrical power generation. Protons are transferred to the cathode through the solid proton conductor (electrolyte) and react with oxygen to produce steam. Essentially, the cogeneration of electricity and ethylene can be achieved in PCFC.

Lin et al. [11] developed an anode consisting of $Co-Cr_2O_3$ nanoparticles as catalyst and $BaCe_{0.8}Y_{0.15}Nd_{0.05}O_{3-\delta}$ as the proton conductor. Their PCFC fed with C_2H_6 obtained a peak power density (PPD) of 173 mW cm^{-2} at 700 °C. The conversion of C_2H_6 reached 34.93 % with a C_2H_4 selectivity of 91.6 %. at 700 °C. The analysis of the outlet gases from the anode showed that methane (< 2.95 %) was the main by-product. In addition, no carbon dioxide and acetylene were detected. Liu et al. [12] reported an efficient anode in which Co nanoparticles were in-situ exsoluted on the perovskite framework. They found the increase of the oxygen vacancy in the material may be beneficial to the catalytic activity of EDH. A maximum output power density of 268 mW cm^{-2} in C_2H_6 at 750 °C was obtained. The yield of C_2H_4 in the PCFC was greatly improved (11.9 %-37.8 %) as the temperature increased from 650 °C to 750 °C. The main by-products in their study are methane and carbon monoxide. Proton-conducting electrolytes may exhibit trace oxygen conductivity at high operating temperatures (> 700 °C), leading to carbon monoxide production [12]. Two different perovskite oxides ($La_{0.6}Sr_{0.4}Fe_{0.9}Nb_{0.1}O_{3-\delta}$, LSFN and $La_{0.6}Sr_{0.4}Fe_{0.8}Nb_{0.1}Cu_{0.1}O_{3-\delta}$, LSFNCu) were synthesized as the catalyst for EDH by Li and co-workers [13]. The results showed that LSFNCu performed better than LSFN since the doped Cu can improve the stability of the catalyst structure and increase oxygen vacancies content. At 750 °C, their PCFC using LSFNCu reached a PPD of 90 mW cm^{-2} and an ethane conversion of 43.4 %. Fan et al. developed another perovskite oxide material with in-situ exsoluted FeNi as the catalyst [14]. At 750 °C, a PPD of 172 mW cm^{-2} and an ethylene yield of 40.5 % were obtained. Notably, no formation of carbon particles or

6

carbon fibers was detected, suggesting good coking resistance of their catalysts.

The above-mentioned studies show the good performance of PCFC and its feasibility in electricity-ethylene cogeneration, however, are all experimental-based. C_2H_6-fueled PCFC involves complex electrochemical/chemical reactions and heat/mass/charge/momentum transport. The interrelationships of these highly coupled processes are difficult to unravel and explain experimentally. Therefore, a cell-level model is necessary to elucidate these complicated multi-physical phenomena. It is still unclear how will the operating parameters such as voltage and flow rates influence the ethylene and power co-generation characteristics. Furthermore, the highly endothermic EDH reaction may cause a local low-temperature zone and a large temperature gradient, which may reduce the local electrochemical performance and reduce the long-term durability of the cell. Given this, it is necessary to incorporate the heat transfer sub-model into the cell-level model to study the thermal behavior during PCFC operation and how the EDH process affects the temperature field within the PCFC. To the authors' best knowledge, no thermo-electrochemical modelling study has been reported on PCFC running on ethane in the open literature. The impacts of different operating parameters on cell performance and the inter-relationships between different operating parameters have not been fully understood yet.

In order to fill the aforementioned research gap, herein, a numerical model is built for a PCFC running on ethane. Detailed parametric studies are performed to obtain a comprehensive insight into the complex physical/chemical/electrochemical processes in C_2H_6-fueled PCFC. The effects of operating parameters (working voltage, inlet fuel flow rate, and inlet temperature) on the PCFC electrochemical and EDH performance are studied. This model provides can serve as a powerful tool to determine suitable operating conditions for PCFC running on ethane.

7

2. Modelling methodology

2.1 Modelling domain and assumptions

A 2D axisymmetric tubular PCFC model is built in the present research. The computation domain, consisting of two gas channels, anode, cathode, and electrolyte, is shown in Figure 1(a). $BaZr_{0.1}Ce_{0.7}Y_{0.2}O_{3-\delta}$ (BZCY) is used as the electrolyte of the cell, while the $(La_{0.6}Sr_{0.4})_{0.95}Fe_{0.8}Ni_{0.1}Mo_{0.1}O_{3-\delta}$ (LSFNM) and $La_{0.6}Sr_{0.4}Co_{0.2}Fe_{0.8}O_{3-\delta}$ (LSCF) serve as anode and cathode, respectively [14]. The geometry parameters are listed in Table 1. Based on our preliminary simulations, it is observed that insufficient chemical reactions in the anode of PCFC can significantly lower cell performance. Therefore, one side of the electrolyte is fully coated by a porous anode layer while the other side of the electrolyte is only partially covered (part of the upstream is uncoated) by the porous cathode layer. With such a design, the upstream section (40 % of the entire cell length) of the PCFC does not involve the electrochemical reaction due to the lack of a cathode. Instead, the upstream section serves as a chemical reactor for EDH reaction to provide sufficient H_2 for subsequent power generation in the PCFC section (60 % of the entire cell length). It is worth noting that in the subsequent content, the internal reforming area (IRA) and the electrochemical reaction area (ERA) are used to represent different regions of the cell. In addition, the thermal cracking reactions are considered to take place in the gas channel, while catalytic chemical reaction occurs in both IRA and ERA. In this study, the ratio of IRA section to ERA section is not optimized. In our subsequent study, this ratio and the other structural parameters will be systematically studied and optimized.
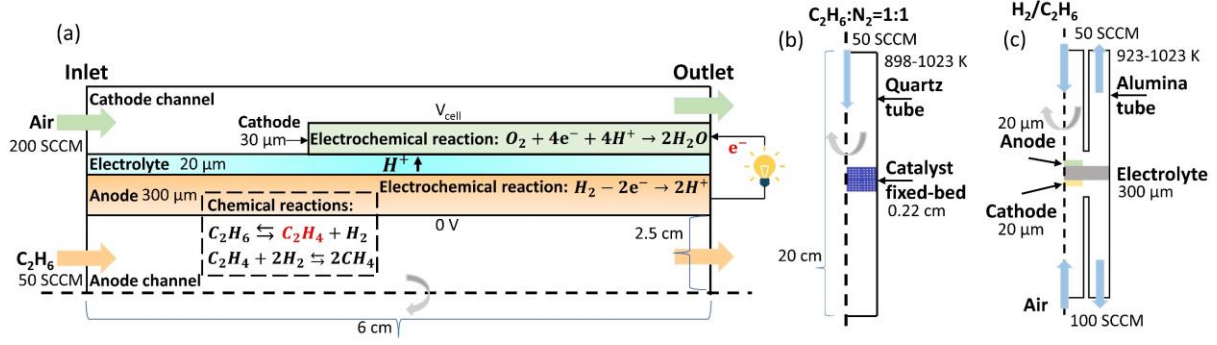
Figure 1 Schematics of (a) a tubular PCFC; (b) a fixed-bed reactor; (c) a button PCFC.

Table 1 Geometrical parameters of tubular PCFC model.

Cell components	Value	Units
Cell length	6	cm
Gas channel width	2.5	mm
Anode thickness	300	μm
Cathode thickness	30	μm
Electrolyte thickness	20	μm

The main assumptions include:

1) The gas species (H_2, O_2, N_2, H_2O, C_2H_6, C_2H_4, CH_4) are considered to be ideal and incompressible gases.

2) The electrode (electronic phase) and the electrolyte particles (protonic phases) are uniformly distributed in the electrodes.

3) The carbon deposition is not considered in this model.

4) Methane is considered the by-product of the chemical reaction.

2.2 Electrochemical model

Since H_2 is considered as the electrochemically active species in this model, the half-electrochemical reactions at the anode side and the cathode side can be written as:

$$Anode\ side: 2H^+ + 2e^- \rightarrow H_2 \tag{1}$$

9

$$Cathode\ side: O_2 + 4H^+ + 4e^- \rightarrow 2H_2O \tag{2}$$
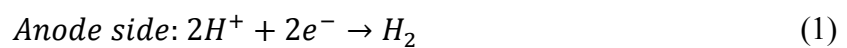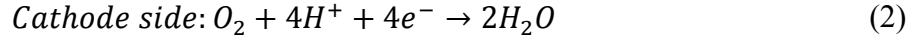
Nernst equation is employed to calculate the equilibrium potential:

$$E_{eq} = E^0 + \frac{RT}{2F} ln\left(\frac{P_{H_2}^l \left(P_{O_2}^l\right)^{0.5}}{P_{H_2O}^l}\right) \tag{3}$$

Where P_i^l is the partial pressure of each gas species (Pa), R is the universal gas constant (8.314 J mol^{-1} K^{-1}), T is the working temperature (K), F is the Faraday constant (96458.3 C mol^{-1}), E^0 is the standard potential can be calculated by [15]:

$$E^0 = 1.253 - 2.4516 \times 10^{-4}T \tag{4}$$

Butler-Volmer equation is adopted to simulate the connection between the local current density (i, A m^{-2}) and activation overpotential (η_{act}, V) [16]:

$$i = i_0\left(exp\left(\frac{\alpha nF\eta_{act}}{RT}\right) - exp\left(\frac{(1-\alpha)nF\eta_{act}}{RT}\right)\right) \tag{5}$$

Where α is the electron transfer coefficient, i_0 represents the exchange current density. The exchange current density at each electrode side can be defined as [17,18]:

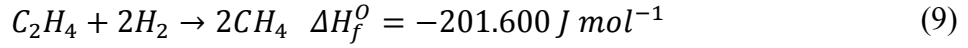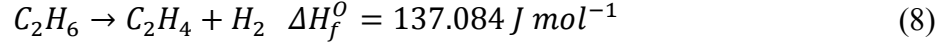$$Anode: i_{0,an} = \gamma_{an}P_{H_2}^l exp\left(-\frac{E_{act,H_2}}{RT}\right) \tag{6}$$

$$Cathode: i_{0,ca} = \gamma_{ca}\left(P_{O_2}^l\right)^{0.21} exp\left(-\frac{E_{act,O_2}}{RT}\right) \tag{7}$$

Where γ_{an} and γ_{ca} represent the pre-factors for the anode and cathode respectively, E_{act} is the activation energy (J mol^{-1}).

2.3 Chemical reaction model

According to the previous experimental study, the thermal cracking of C_2H_6 in the gas channel evidently imposes an effect on the conversion of C_2H_6 [19]. Thus, the thermal cracking of C_2H_6 in the gas channel as well as the catalytic reaction of C_2H_6 on the catalytic sites in the porous anode layer are taken into account in this model. It is worth noting that, methane formation

10

(MF) primarily originates from the dissociation of the C-C bond in C_2H_4 based on the isotopic tracer studies from the literature [20]. Thereupon, the following reactions are considered in the model:

$$C_2H_6 \rightarrow C_2H_4 + H_2 \quad \Delta H_f^0 = 137.084 \, J \, mol^{-1} \tag{8}$$

$$C_2H_4 + 2H_2 \rightarrow 2CH_4 \quad \Delta H_f^0 = -201.600 \, J \, mol^{-1} \tag{9}$$

The reaction rates (mol m^{-3} s^{-1}) of the above two reactions are given as follows:

$$R_{EDH} = k_1 \left[y_{C_2H_6} \left(\frac{P_t}{RT} \right) - \frac{y_{C_2H_4} y_{H_2}}{K_{eq1}} \left(\frac{P_t}{RT} \right)^2 \right] \tag{10}$$

$$R_{MF} = k_2 \left[y_{C_2H_4} (y_{H_2})^2 \left(\frac{P_t}{RT} \right)^3 - \frac{(y_{CH_4})^2}{K_{eq2}} \left(\frac{P_t}{RT} \right)^2 \right] \tag{11}$$

Where y_i is the molar fraction for each gas species (mol s^{-1}), P_t is the total pressure (Pa), k_i is the kinetic rate constant for each reaction, can be further expressed as:

$$k_{therm \, EDH} = k_{1 \, therm}^0 exp \left(-\frac{E_{act,therm \, EDH}}{RT} \right) \tag{12}$$

$$k_{cata \, EDH} = k_{1 \, cata}^0 exp \left(-\frac{E_{act,cata \, EDH}}{RT} \right) \tag{13}$$

$$k_{MF} = k_2^0 exp \left(-\frac{E_{act,MF}}{RT} \right) \tag{14}$$

Where k_r^0 is the pre-exponential factor for each rate constant, $E_{act,r}$ is the activation energy for each chemical reaction (J mol^{-1}). The parameters in the rate expressions are based on the literature [21–25].

2.4   Charge transport

Ohm's law is implemented to describe the transport of protons/electrons [26]:

$$\nabla \cdot \boldsymbol{i}_p = \nabla \cdot \left(-\sigma_{p,eff} \nabla \phi_p \right) = -i_0 l_{TPB} \tag{14}$$

$$\nabla \cdot \boldsymbol{i}_e = \nabla \cdot \left(-\sigma_{e,eff} \nabla \phi_e \right) = i_0 l_{TPB} \tag{15}$$

11

Where i_k is the current vector of each charge species (A m^{-2}), ϕ_k is the potential of the protonic/electronic phase (V), l_{TPB} is the reaction area at the triple phase boundary (m^2 m^{-3}), $\sigma_{k,eff}$ is the effective conductivity of each charge species (S m^{-1}), which can be expressed as:

$$\sigma_{p,eff} = \sigma_{0,p} \cdot \frac{V_p}{\tau_p} \tag{16}$$

$$\sigma_{e,eff} = \sigma_{0,e} \cdot \frac{V_e}{\tau_e} \tag{17}$$

Where $\sigma_{0,k}$ is the intrinsic conductivity of each charge species (S m^{-1}), V_k is the volume fraction of the protonic/electronic phase, τ_e is the tortuosity of the protonic/electronic phase.

2.5 Mass and momentum transport

The above-mentioned rate expressions are used to calculate the source terms added to the mass conservation equation, while Darcy's term modified Navier-Stokes equation is implemented to describe the momentum transport in the porous media [27].

$$\rho \nabla \cdot \boldsymbol{u} = Q_m = \sum y_i R_i \tag{18}$$

$$\frac{\rho}{\varepsilon} (\boldsymbol{u} \cdot \nabla) \cdot \frac{\boldsymbol{u}}{\varepsilon} = -\nabla P + \nabla \cdot \left[\frac{\mu}{\varepsilon} (\nabla \boldsymbol{u} + \nabla \boldsymbol{u}^T) - \frac{2}{3} \frac{\mu}{\varepsilon} (\nabla \cdot \boldsymbol{u}) \right] - \left(\mu \kappa^{-1} + \frac{Q_m}{\varepsilon^2} \right) \boldsymbol{u} \tag{19}$$

Where $\boldsymbol{u}$ is the velocity vector (m s^{-1}), ρ is the density (kg m^{-3}), y_i is the mole fraction of each species, μ is the viscosity (Pa s), P is the operating pressure (Pa), κ is the permeability (m^2), ε is the porosity of the media. It should be noted that, in the non-porous gas channel, the porosity is set as unity while Darcy's term is omitted. The density as well as the viscosity of the gas mixtures are expressed as:

$$\rho = \frac{P}{RT} \sum_i \frac{\omega_i}{M_i} \tag{20}$$

$$\mu = \sum_i \frac{y_i \mu_i}{\sum_j y_j \varphi_{ij}} \tag{21}$$

12

$$\varphi_{ij} = \frac{1}{\sqrt{8}} \left(1 + \frac{M_i}{M_j}\right)^{-1/2} \left[1 + \left(\frac{\mu_i}{\mu_j}\right)^{1/2} \left(\frac{M_j}{M_i}\right)^{1/4}\right]^2 \qquad (22)$$

Where ω_i is the mass fraction of each gas species, μ_i is the viscosity of each gas species (Pa s), M_i is the molar mass of each gas species (kg mol^{-1}), φ_{ij} is the inter-collisional parameter [28].

The dust gas model is applied in this study to simulate molecular diffusion and Knudsen diffusion in porous media [29]. Noteworthy, the Knudsen diffusion of gas species is neglected in the flow channel.

$$\frac{N_i}{D_{iK}^{eff}} + \sum_{j=1}^{n} \frac{y_j N_i - y_i N_j}{D_{ij}^{eff}} = -\frac{1}{RT} \left(P \nabla y_i + y_i \nabla P + y_i \nabla P \frac{kP}{D_{iK}^{eff} \mu}\right) \qquad (23)$$

Where N_i is the molar flux of each species (mol m^{-2} s^{-1}), D_{iK}^{eff} is the effective Knudsen diffusion coefficient of species i (m^2 s^{-1}) and can be expressed as [28]:

$$D_{iK}^{eff} = \frac{\varepsilon}{\tau} \frac{2}{3} r_p \sqrt{\frac{8RT}{\pi M_i}} \qquad (24)$$

Where r_p is the radius of pores (m). D_{ij}^{eff} is the effective binary diffusion coefficient (m^2 s^{-1}) and can be written as:

$$D_{ij}^{eff} = \frac{\varepsilon}{\tau} \cdot D_{ij}^0 \qquad (25)$$

Where D_{ij}^0 is the binary molecular diffusion coefficient (m^2 s^{-1}) determined by a modified Chapman-Enskog relation [28,30–32]:

$$D_{ij}^0 = \frac{0.042851 \times \left(\frac{1}{M_i} + \frac{1}{M_j}\right)^{-0.5} - 0.0098 \times T^{1.5}}{P \Omega_D \sigma_{ij}^2} \qquad (26)$$

$$\Omega_D = A(T^*)^B + C\,exp(DT^*) + E\,exp(FT^*) + G\,exp(HT^*) \qquad (27)$$

$$T^* = \frac{T}{\varepsilon_{ij}} \tag{28}$$

$$\varepsilon_{ij} = \sqrt{\varepsilon_i \varepsilon_j} \tag{29}$$

$$\sigma_{ij} = \frac{1}{2}(\sigma_i + \sigma_j) \tag{30}$$

Where Ω_D is the temperature-dependent collision integral, T_b is the boiling temperature at the standard air pressure (K), A to H are the empirical constants that can be obtained from the literature [33,34].

2.6   Heat transport

Both electrochemical reactions and chemical reactions could considerably influence the temperature field in the cell. Meanwhile, based on Eq. (12)-(14), the reaction rates are intrinsically related to the temperature. Thereby, it is important to simulate the heat transport in channels and porous media. The energy conservation equation is expressed as [17]:

$$\rho C_p \boldsymbol{u} \nabla T + \nabla \cdot \left(-k_{eff} \nabla T\right) = Q_H \tag{31}$$

Where C_p is the specific heat capacity (J kg^{-1} K^{-1}), k_{eff} is the effective thermal conductivity (W m^{-1} K^{-1}).

$$C_p = \sum_i y_i \cdot C_{p,i} \tag{32}$$

$$k_{eff} = \varepsilon \cdot k_g + (1 - \varepsilon) \cdot k_s \tag{33}$$

$$k_g = \sum_i y_i \cdot k_i \tag{34}$$

Where $C_{p,i}$ is the specific heat of each gas species (J kg^{-1} K^{-1}), k_s represent the solid phase heat conductivity (W m^{-1} K^{-1}), k_i denotes the gas species thermal conductivity (W m^{-1} K^{-1}), Q_H represents the heat source or sink [35,36]. The heat source for electrochemical reactions, chemical reactions, and ohmic heat could be determined as listed:

$$Q_{elec} = (-T\Delta S) \cdot \frac{i}{nF} \qquad (35)$$

$$Q_{chem} = R_r \Delta H_r \qquad (36)$$

$$Q_{ohmic} = -(i \cdot \nabla \phi) \qquad (37)$$

Where ΔS represents the change of entropy of the electrochemical reaction (J mol^{-1} K^{-1}), ΔH_r represents the change of enthalpy of the chemical reactions (J mol^{-1}).

Table 2 Parameters adopted in the model.

Parameters	Value or expression	Unit	Refs
$E_{act,an}$	1.2×10^5	J mol^{-1}	[37]
$E_{act,ca}$	1.3×10^5	J mol^{-1}	[37]
γ_{an}	1.5×10^9		
γ_{ca}	7×10^8		
$\sigma_{LSFNM,a}$	$5.6 \times 10^5 exp(-4540/T)/T$	S m^{-1}	[14]
$\sigma_{BZCY,ele}$	$290.4 exp(-4600.6/T)$	S m^{-1}	[38]
$\sigma_{LSCF,ca}$	$(100/T)10^{4.32575+\frac{1204.26}{T}}$	S m^{-1}	[40]
ε_{an}	0.4		[14]
ε_{ca}	0.4		
τ	3		[40]
P	1	atm	
T_{op}	923-973	K	
κ	1.70×10^{-10}	m^2	[39]
l_{TPB}	2.14×10^5	m^2 m^{-3}	[40]
$x_{an,inlet}$	Pure C_2H_6		
$x_{ca,inlet}$	Air		
$v_{an,inlet}$	50	SCCM	
$v_{ca,inlet}$	200	SCCM	
V_{cell}	0.55	V	

2.7 Boundary conditions and model validation

Table 2 summarizes the input parameters. It is worth noting that the inlet air flow rate is set to provide sufficient air to the cathode and avoid the electrochemical performance at the cathode from being compromised by oxygen depletion. However, a too high air flow rate may cause more energy consumption, which may reduce the net power generation from the fuel cell. For particular applications, the flow rate must be carefully determined to achieve the best system performance. Table 3 lists all the boundary conditions. Before the parametric studies, the validation of the model is necessary. The modelling simulation is implemented by the finite element method (COMSOL Multiphysics). The operating conditions used in the validations are collected in Table 4. A 2D fixed-bed reactor model (Figure 1 (b)) is constructed to verify the chemical reaction. The chemical reaction kinetics is validated based on the ethane conversion and ethylene selectivity, two of which are compared with the experimental results from the literature [19]. The expressions of ethane conversion and ethylene selectivity are shown as follows:

$$Ethane\ converison, X_{C_2H_6} = \frac{F_{C_2H_6,in} - F_{C_2H_6,out}}{F_{C_2H_6,in}} \times 100\% \tag{38}$$

$$Ethylene\ selectivity, S_{C_2H_4} = \frac{F_{C_2H_4,out}}{F_{C_2H_6,in} - F_{C_2H_6,out}} \times 100\% \tag{39}$$

Table 3 Boundary conditions of the model.

Location	Boundary conditions (Charge, mass, momentum, energy)
Anode inlet	$x_{an,inlet}, v_{an,inlet}, T_{op}$
Cathode inlet	$x_{ca,inlet}, v_{ca,inlet}, T_{op}$
Anode upper-face	$\varphi_e = 0$
Cathode upper-face	$\varphi_e = V_{cell}$
Anode outlet	Open boundary

| Cathode outlet | Open boundary |
| Other boundaries | Insulation/Wall |

Table 4 Operating conditions in the validation process.

Descriptions	Fixed-bed reactor model [19]	Button cell
Inlet/anode inlet	$C_2H_6:N_2=1:1$	H_2 or C_2H_6
Cathode inlet	—	Air
Operating temperature	898-1023 K	923, 973, 1023
Operating pressure	1 atm	1 atm
Inlet/anode inlet flow rate	50 SCCM	50 SCCM
Cathode inlet flow rate	—	100 SCCM
Voltage	—	OCV-0.2 V

The good agreement in Figure 2(a) verifies the accuracy of the adopted chemical reaction kinetics under the condition either with the catalyst or without the catalyst. A PCFC button cell model (shown in Figure 1(c)) is constructed to validate the electrochemical model. The geometry of the button cell and inlet conditions are based on the experiment [14]. The electrochemical performance of H_2 feed and C_2H_6 feed PCFC button cell are validated, respectively. Good agreements between the simulation results and the experimental data are shown in Figure 2 (b) and (c) [14]. The mesh independence is obtained at 103422 DOF and 26051 meshing elements. The current density difference with the further increased mesh is less than 0.1%.
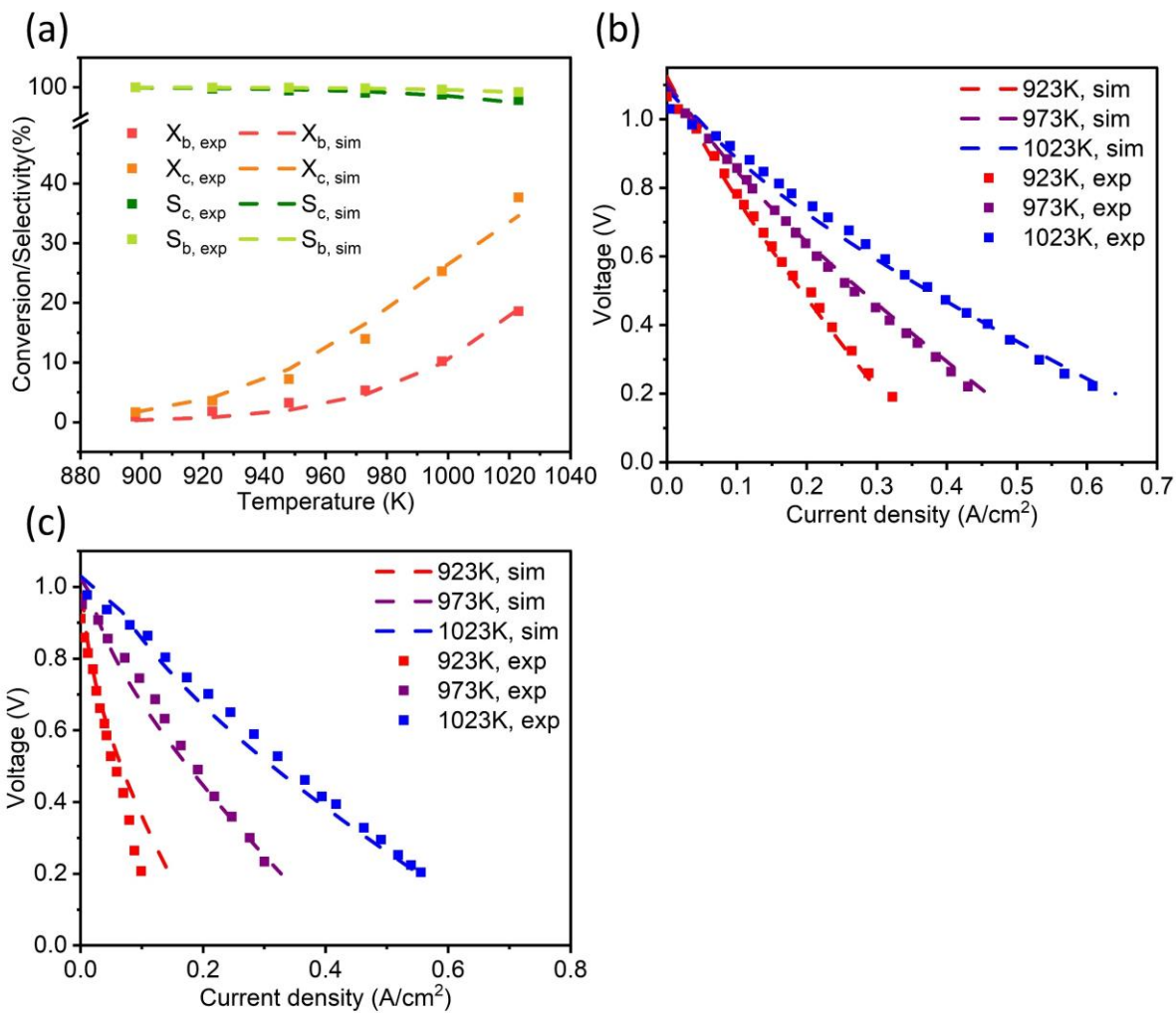
Figure 2 The validation of (a) the chemical reaction in the fixed-bed reactor model; (b) the electrochemical model with H_2 as anode fuel in the button cell model; (c) the electrochemical model with C_2H_6 as anode fuel in the button cell model.

3. Results and discussion

3.1 OCV condition
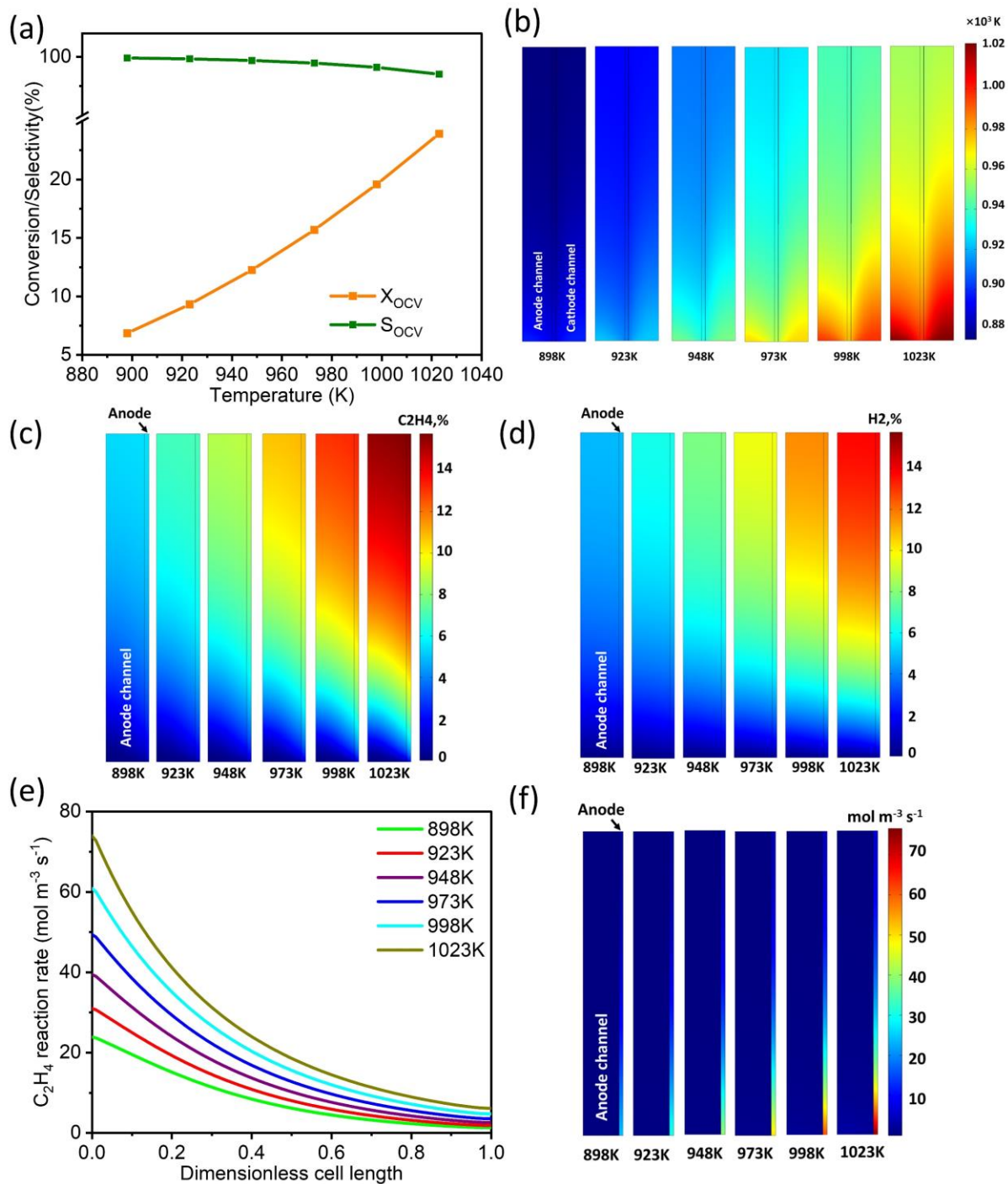
Figure 3 (a) The conversion/selectivity under the OCV; (b) the temperature distribution in the whole cell; (c) C_2H_4 molar fraction distribution in the anode gas channel and anode; (d) H_2 molar fraction distribution in the anode gas channel and anode; (e) the reaction rate of C_2H_4 distribution in the anode along the cell length; (f) the reaction rate of C_2H_4 distribution in the anode gas channel and anode.

In order to show the electrochemical reaction's positive effects on the EDH process, a base

19

case of PCFC operating under the OCV condition is essential. Therefore, the study is conducted by varying the operating temperature between 898 K and 1023 K. In Figure 3(a), C_2H_6 conversion under OCV is markedly improved by increasing the temperature, while C_2H_4 selectivity demonstrates a slight negative relation to temperature increase. Specifically, when the temperature is adjusted from 898 K to 1023 K, the conversion increases from 6.86 % to 23.91 %, while the selectivity decreases from unity to 98.51 %. The temperature decreases from the inlet to the outlet (Figure 3(b)). It shows the significant endothermic effects of Eq. (8). In addition, the temperature gradient increases with the increase in temperature.

Figure 3(c) and (d) show that both C_2H_4 molar fraction and H_2 molar fraction increase along the cell. The molar fractions of outlet H_2 and C_2H_4 at 1023 K are nearly triple those at 898 K. The reaction rate of C_2H_4 decreases continuously from the inlet to the outlet (Figure 3(e)), while the global distribution of reaction rate in the anode (Figure 3(f)) suggests that the reaction rate in the anode layer is more notable than that in the anode flow channel, denoting the irreplaceable role that catalyst layer plays in the EDH process. Furthermore, temperature considerably influences the extent of reaction. Specifically, a tremendous 200 % enhancement in the inlet reaction rate is observed when the temperature increases from 898 K to 1023 K.

3.2 Effects of operating voltage

The operating voltage of PCFC is adjusted from 0.9 V to 0.2 V. The effects of the operating voltage on PCFC electrochemical performance are shown in Figure 4(a). The PPD at 923 K is only 71.27 mW cm^{-2}, while it reaches 146.12 mW cm^{-2} at 973 K. Figure 4(b) shows that C_2H_6 conversion and C_2H_4 selectivity reach 51.83 % and 94.80 % at 973 K, respectively. With the decrease of operating voltage, C_2H_6 conversion increases monotonously, while C_2H_4 selectivity shows a slight negative correlation. Compared with Figure 3 (a), Figure 4 (b) indicates that, although the drop in C_2H_4 selectivity at 0.4 V becomes more significant at high operating temperature compared to the OCV condition, both C_2H_6 conversions are improved significantly.

20

Therefore, it suggests the electrochemical reaction in the PCFC can significantly enhance the EDH process, subsequently achieving the cogeneration of electric power and ethylene.
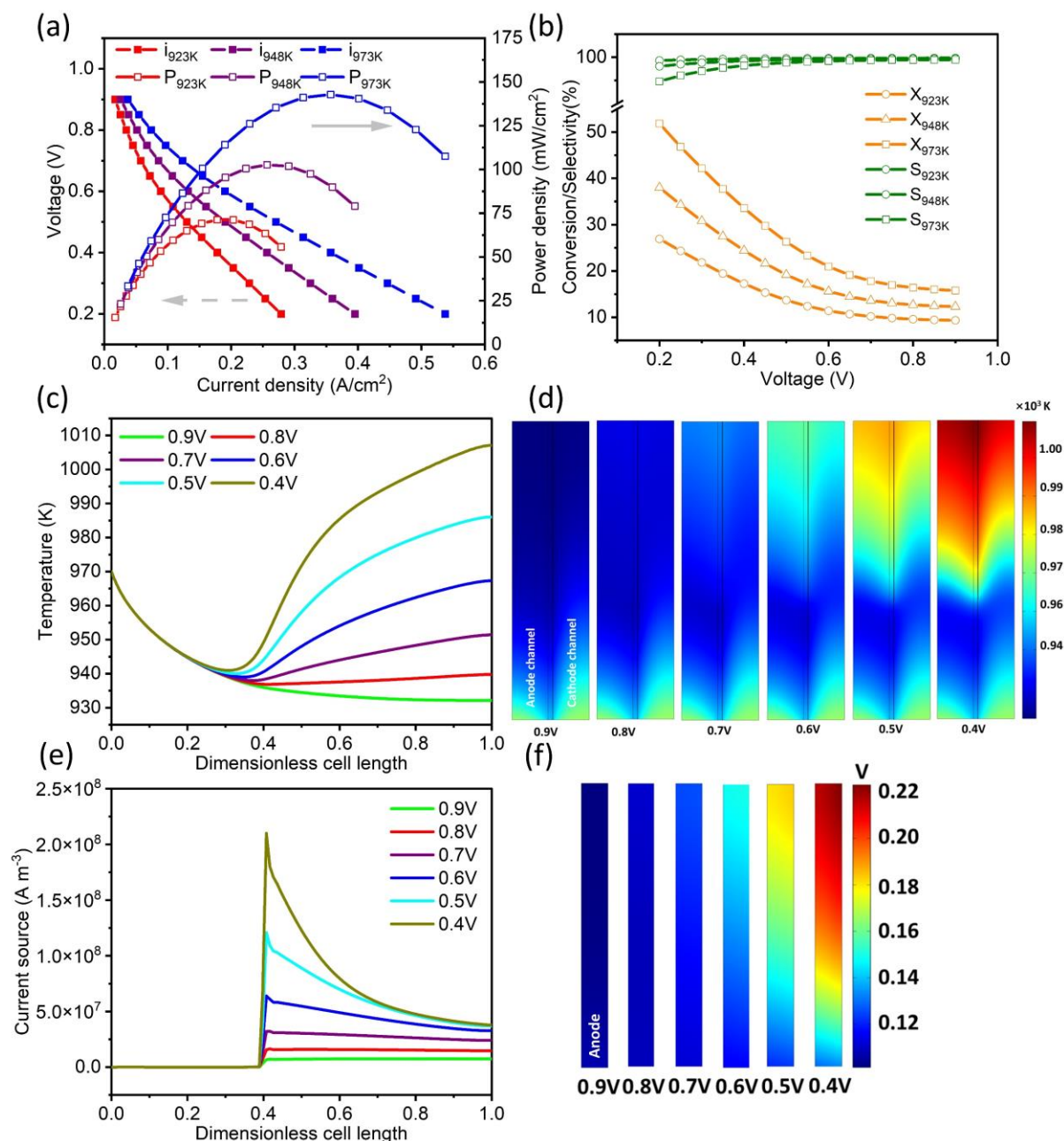

Figure 4 The effects of operating voltage (a) on the power density and current density; (b) on the C_2H_6 conversion and C_2H_4 selectivity; (c) on the temperature distribution in the anode gas channel along the cell length; (d) on the temperature distribution in the whole PCFC; (e) on the current sources distribution at the anode-electrolyte interface along the cell length; (f) on the concentration loss distribution in the ERA of the anode.

In Figure 4(c) and (d), the temperature drops in the IRA and increases in the ERA except for the profiles at 0.9 V. The temperature increase in ERA can be attributed to the exothermic

electrochemical reaction. However, for the curve at 0.4 V, it can be found that the slope of the temperature increase decreases significantly (dimensionless element length > 0.6). This implies that the electrochemical reaction weakens considerably in this region, which is also evidenced by Figure 4(e). Furthermore, the temperature gradient in the ERA (up to 16.6 K cm^{-1} at 0.4V) also increases with the decrease of operating voltage. The operating voltage should be carefully controlled to avoid such a high temperature gradient in the PCFC, thus guaranteeing safe operation. Figure 4(e) shows that there are no current sources in the IRA, while the current sources increase in the ERA and are distributed more unevenly with the decrease of operating voltage. As mentioned before, when dimensionless cell length > 0.7 and at 0.4 V, the electrochemical reaction is considerably weakened, and its value stands nearly the same as the 0.5 V. Additionally, this indicates that almost 50% of ERA underperforms as expected. This is caused by the hydrogen depletion in the anode layer. As shown in Figure 4(f), as the operating voltage decreases, the concentration overpotential in the anode ERA (especially near the outlet) increases, which is detrimental to the local electrochemical performance.

As shown in Figure 5(a) and (b), the C_2H_4 reaction rate in most of IRA is nearly unaffected by the operating voltage. The C_2H_4 reaction rate in the region near the ERA increases with the decrease of working voltage, which can be ascribed to the heating effects of the electrochemical reactions in the ERA. In addition, when operating voltage < 0.6 V, the C_2H_4 reaction rate starts to increase in the ERA as the electrochemical consumption of H_2 shifts the equilibrium of Eq. (8) to the right-hand side. Noteworthy, EDH at the anode-electrolyte interface side is more intensive than that at the anode-channel interface side. Several potential reasons are listed here: 1) At the anode-electrolyte interface side, the H_2 generated from EDH is consumed at the TPB. The H_2 consumption can significantly promote the ethane dehydrogenation reaction. In addition, the thickness of the electrochemical-active area in the anode is typically around 5 μm to 10 μm [41]. Thus, the electrochemical oxidation of H_2 at the anode-electrolyte interface side

22

enables EDH more intensively; 2) Although the concentration of C_2H_6 at the anode-channel interface side is higher than that at the anode-electrolyte interface side, its effect on EDH is negligible relative to H_2 electrochemical consumption due to the thin anode thickness; 3) EDH is an inherently endothermic process. Therefore, the heat released by the electrochemical reaction and ohmic heat generated by the charge transport in the electrolyte favour ethane dehydrogenation. Consequently, from the perspective of thermodynamics, the EDH at the anode-electrolyte interface side is more intensive than that at the anode-channel interface side. Figure 5(c) and (d) imply that both H_2 molar fraction and C_2H_4 molar fraction in most of IRA are virtually not dependent on the operating voltage. In the ERA, the H_2 mole fraction decreases significantly with decreasing operating voltage. Meanwhile, the electrochemical consumption of H_2 promotes the conversion of C_2H_6, leading to the increase of C_2H_4 molar fraction in the ERA. In addition, it can be found that the H_2 molar fraction in the half of ERA remains at a relatively low-level (< 1 %) when operating voltage < 0.5 V, subsequently leading to the deterioration of local electrochemical performance. To address the H_2 depletion issue in the PCFC fed with C_2H_6, it is desirable to enhance to EDH reaction for H_2 generation. Optimization of the IRA/ERA ratio and optimization of the porous layer are possible ways to achieve high performance of the PCFC, which will be the focus our subsequent study. In Figure 5(e), as the operating voltage decreases, the net heat generation increases monotonously. The heat generated from the cathode is a key engine of the growth of net heat. The substantial cooling effects of the endothermic chemical reaction are shown in Figure 5(f), while the decreasing operating voltage enables the continuous increase of heat generation from the ohmic overpotential as well as the electrochemical reaction, compensating for the heat absorbed by the EDH process.

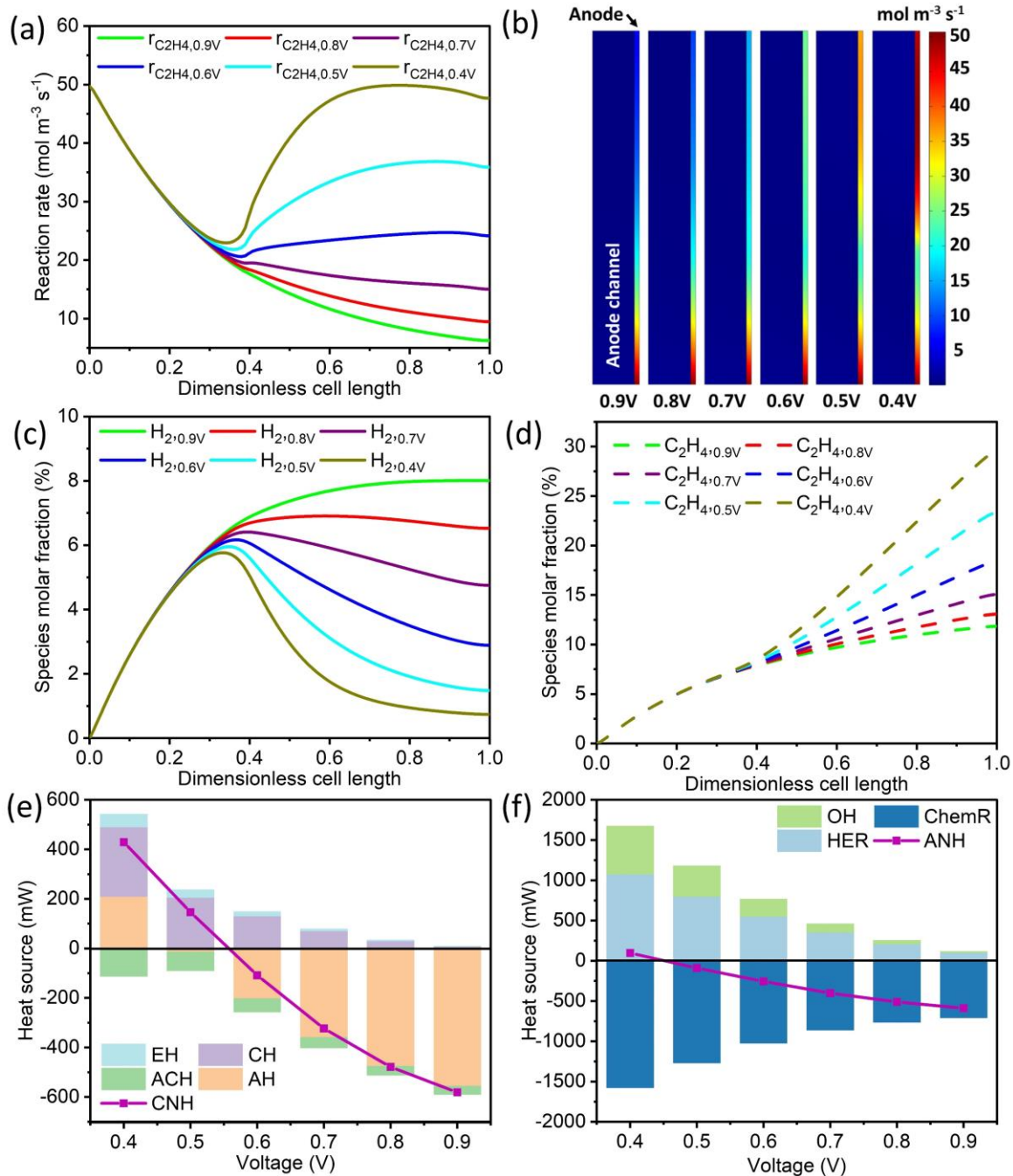Figure 5 The effects of operating voltage (a) on the C_2H_4 reaction rate distribution in the anode along the cell length; (b) on the reaction rate distribution of C_2H_4 in the anode gas channel and anode; (c) on the molar fraction of H_2 in the anode along the cell length; (d) on the molar fraction of C_2H_4 in the anode along the cell length; (e) on the heat sources from different components of PCFC; (f) on the different heat sources in the anode and anode gas channel. EH: electrolyte heat source, which means the ohmic heat released from the electrolyte; CH: cathode heat source, which consists of ohmic heat, irreversible heat of electrochemical reduction of O_2; ACH: anode channel heat source, which is the heat absorbed by the thermal cracking reactions in the anode gas channel; AH: anode heat source, which consists of ohmic heat, irreversible heat of electrochemical oxidation of H_2 and heat adsorbed by catalytic chemical reactions; CNH: cell net heat source, which represent the total net heat released by the whole PCFC; OH: ohmic heat source, which includes all the heat generated by ohmic loss; HER: hydrogen electrochemical reaction heat source, which accounts the irreversible heat released by

electrochemical reaction in the PCFC, ChemR: chemical reaction heat source, which accounts the heat adsorbed by all chemical reactions in the PCFC, ANH: anode side net heat source, which represents the total heat released from the anode side of PCFC.
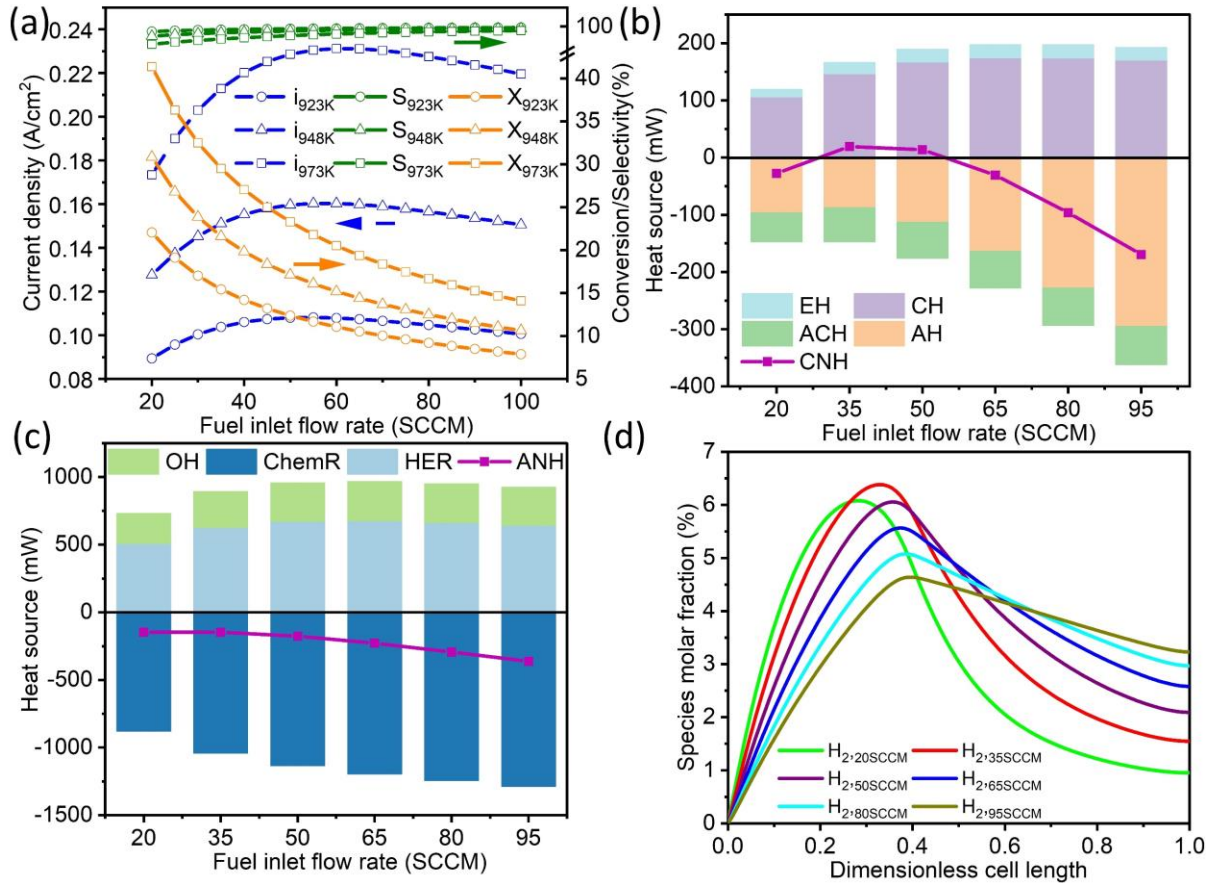
3.3 Effects of inlet fuel flow rate

Figure 6 The effects of inlet fuel flow rate (a) on the current density, C_2H_6 conversion, and C_2H_4 selectivity; (b) on the heat sources from different components in the cell; (c) on the different heat sources in the anode and anode gas channel; (d) on the molar fraction of H_2 in the anode along the cell length.

The inlet fuel flow rate is capable to control the residence time of C_2H_6 in the PCFC, which in turn poses a certain impact on the EDH performance and electrochemical performance of the PCFC. Therefore, the inlet fuel flow rate is an important operating parameter to the cogeneration performance of PCFC, and it is of great value to study its impacts. In this sub-study, the anode inlet flow rate is changed in the range between 20 and 100 SCCM to study the effects of inlet fuel flow rate. In Figure 6(a), the C_2H_6 conversion profiles at different temperatures show a similar trend, i.e., it declines continuously with the increase of the inlet

25

fuel flow rate. Meanwhile, C_2H_4 selectivity shows the inverse trend. The impacts of inlet fuel flow rate on the C_2H_6 conversion and C_2H_4 selectivity become more pronounced with the increase in the operating temperature. The increase in fuel load with increasing inlet fuel flow may be responsible for the initial increase in current density. However, with a further increase in the fuel inlet flow, the decreased C_2H_6 conversion inevitably results in a decrease in the H_2 mole fraction in the inlet of ERA (Figure 6(d)). Furthermore, at the high inlet fuel flow rate, the heat generated by the HER is rapidly carried away (Figure 6(c)), meanwhile, the faster chemical reaction absorbed more heat at the anode side. Hence, it makes CNH negative (Figure 6(b)) and reduces the temperature in the ERA, eventually leading to lower electrochemical performance. This analysis shows that multi-physics phenomena are inter-coupled as well as interact with one another. Hence, it is paramount to develop a model to reveal their complex interrelationships. The fuel flow rate should be carefully controlled to achieve a balance between power generation and ethylene production abilities.
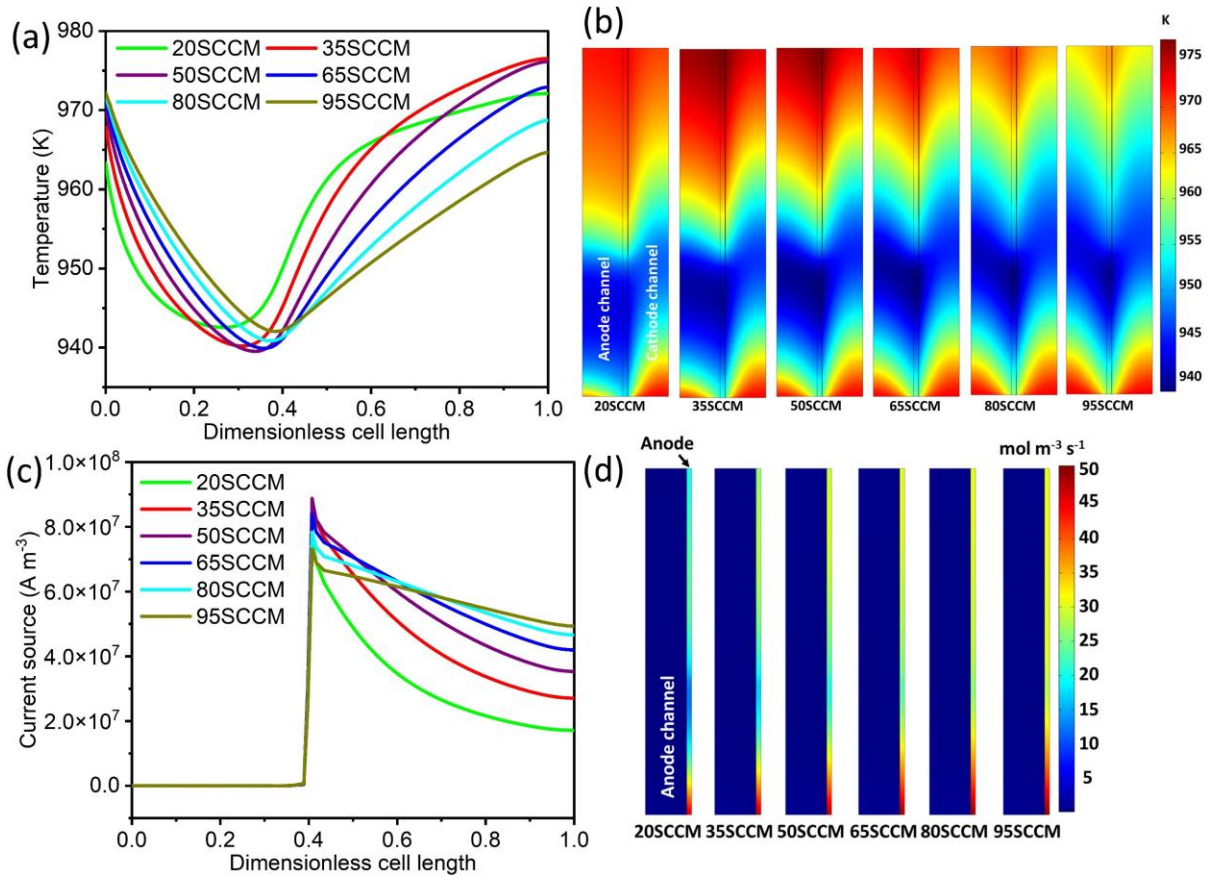
Figure 7 (a) on the temperature distribution in the anode gas channel along the cel length; (b) on the temperature distribution in the whole PCFC; (c) on the current sources distribution at the anode-electrolyte interface along the cell length; (d) on the C_2H_4 reaction rate distribution in the anode gas channel and anode.

In Figure 7(a), the temperature decreases in the IRA and increases in the ERA. As the inlet fuel flow rate increases, the lowest temperature position starts to move towards the outlet direction. This could be explained by the following possible reasons: 1) with the increase in fuel flow rate, more amount of C_2H_6 requires more reaction area to reach the equilibrium, enlarging the temperature cooling zone (Figure 7(b)); 2) high velocity in the anode channel brings better thermal convection, leading to more uniform temperature distribution. As the inlet fuel flow rate increases, the value of the lowest temperature initially decreases due to the increasing endothermic reaction rate leading to pronounced cooling effects. The remarkable cooling zone can be observed at 50 and 65 SCCM (Figure 7 (b)). With the further increase in flow rate, the value of the lowest temperature increases since a high flow rate brings reduced C_2H_6 conversion, which means equilibrium is easier to obtain in the IRA and makes a more uniform

temperature distribution in the IRA. Furthermore, in the ERA, the peak temperature initially rises with the increase of fuel flow rate (Figure 7(a) and (b)) as increased H_2 molar fraction enhances the electrochemical reaction resulting in higher heat generation (Figure 6(a) and (b)). Then, the peak temperature decreases since 1) high thermal convection brought by a high flow rate makes temperature distribute in the ERA more evenly, 2) heat consumption caused by the endothermic reaction becomes more tremendous (Figure 6(b)).

In Figure 7(c), as the flow rate increase from 20 to 50 SCCM, the current sources are considerably enhanced in the ERA. The change in current source distribution at flow rates > 50 SCCM is the result of the dual effects of local temperature and local H_2 mole fraction. Specifically, combing Figure 6(d) and Figure 7(a), when dimensionless cell length < 0.6, the current source drops with increasing inlet flow rate due to both decreased temperature and H_2 mole fraction. In the rest of the ERA region, as the inlet flow rate increases, the increase in H_2 mole fraction eventually leads to an increase in the current source despite the decrease in temperature. In Figure 7(d), the high reaction rate region in the cell inlet enlarges due to the increase of local temperature (Figure 7(a)) with the increasing inlet flow rate. In addition, the C_2H_6 reaction rate is more uniform as the flow rate increases.

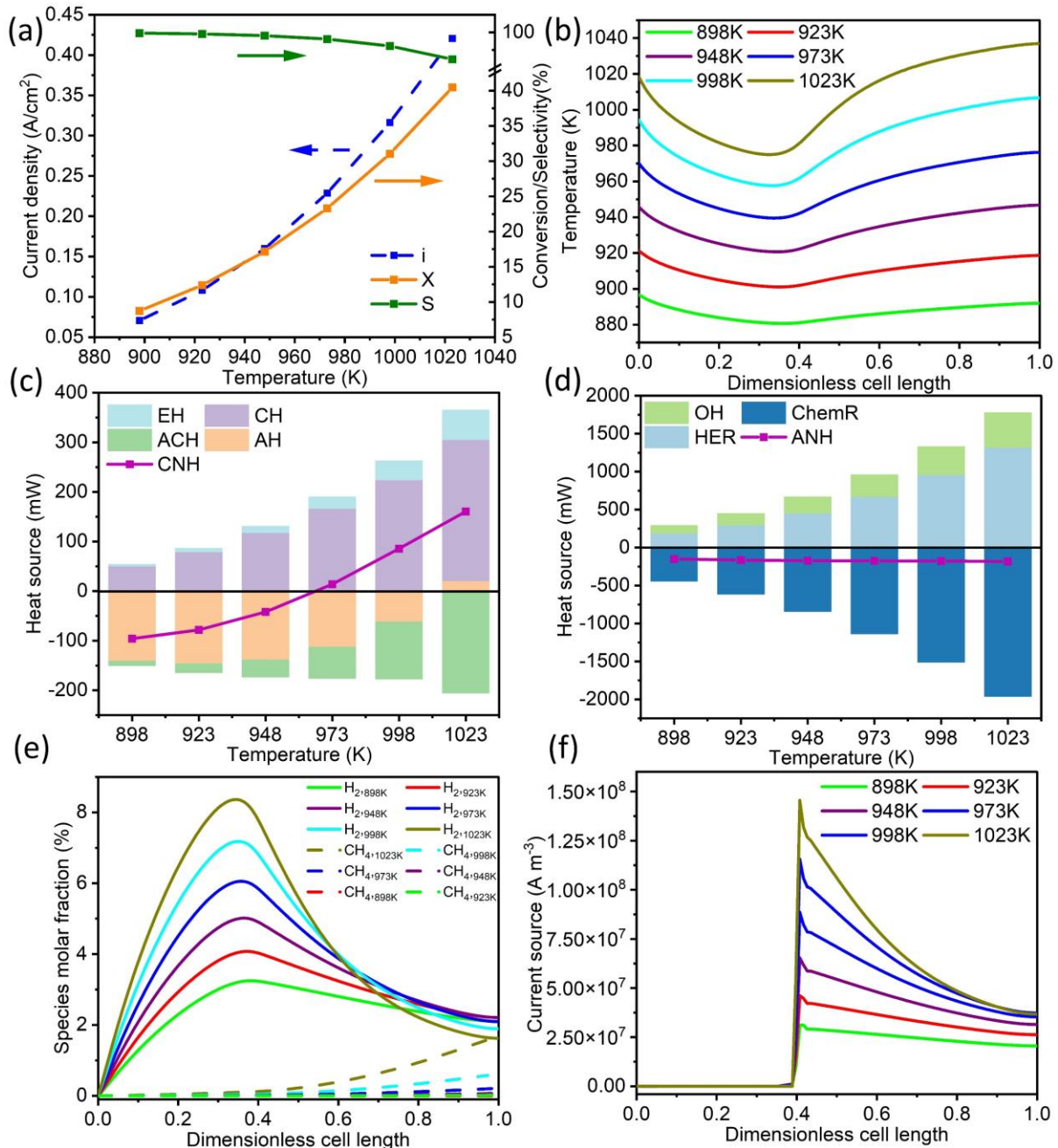## 3.4   Effects of inlet temperature

Figure 8 The effects of inlet temperature (a) on the current density, C_2H_6 conversion, and C_2H_4 selectivity; (b) on the temperature distribution in the anode gas channel along the cell length; (c) on the heat sources from different components; (d) on the different heat sources in the anode and anode gas channel; (e) on the H_2 molar fraction and CH_4 molar fraction in the anode along the cell length; (f) on the current sources distribution at the anode-electrolyte interface along the cell length.

The inlet temperature is intrinsically related to the kinetics of both chemical and electrochemical reactions. Consequently, it is significant to investigate the influences of inlet temperature on the cogeneration capacity of PCFC. In this sub-study, the inlet temperature of

29

both anode and cathode gas channels are synchronously varied between 898 K and 1023 K. In Figure 8(a), both C_2H_6 conversion and current density are positively correlated with the increase of inlet temperature, reaching the value of 40.48 % and 0.42 A cm^{-2} respectively at 1023 K. Meantime, C_2H_4 selectivity decreases from the unity to 95.1 %. With increasing inlet temperature, Figure 8(b) shows that the temperature gradient increases in both IRA and ERA. The difference in the temperature gradient in the IRA with the increase in inlet temperature is the result of the endothermic reaction (Figure 8(d) and (e)). The variation in the temperature gradient in the ERA with the increase of inlet temperature is caused by the increased heat generation from electrochemical reaction and ohmic overpotential (Figure 8(d) and (e)). Based on Eqs. (6), (7) and (12-14), the temperature has an exponential effect on the kinetics of electrochemical and chemical reactions. Therefore, a change in inlet temperature results in a more pronounced variation in the temperature distribution in the PCFC compared to the inlet fuel flow (Figure 8(b)). The CNH starts to become positive when the inlet temperature is > 973 K. The inlet temperature should be carefully controlled to avoid the endothermic operation of the cell and high temperature gradient.

As shown in Figure 8(e), when the inlet temperature increases, the difference in H_2 molar fraction in the IRA increases due to the high C_2H_6 conversion. While H_2 molar fraction declines more significantly owing to the faster electrochemical reaction (Figure 8(f)) with the increase of inlet temperature. When the dimensionless cell length > 0.6, the mole fraction of H_2 at 998 K and 1023 K is even lower than that at 973 K. Noteworthy, the decrease in the H_2 molar fraction with the inlet temperature at 1023 K results in the reduction of the local electrochemical performance of 50 % of ERA to the same level as that at 998 K (Figure 8(f)). As a consequence, although the overall electrochemical performance is the best at 1023 K, how to prevent H_2 depletion and improve local electrochemical performance can be the main focus of future studies. As discussed earlier, the cogeneration performance of PCFC can be enhanced

30

by increasing temperature. However, the working temperature cannot be unlimitedly increased in practical operation. First, the increased temperature can induce the increased generation of by-products (Figure 8(a)). Second, the equilibrium potential of C_2H_6-fed PCFC is weakened by increasing working temperature. Third, under a working high temperature, the start-up of PCFC is time- and energy- expensive, and the requirements of materials become more stringent. Consequently, the working temperature should be well-controlled in practical operation. Additionally, the CH_4 molar fraction distribution is shown in Figure 8(e). When the inlet temperature is > 998 K, the carbon deposition induced by methane cracking is thermodynamically possible. Therefore, the inlet temperature should be controlled to prevent carbon deposition.

4. Conclusions

In this work, a mathematical model is constructed to simulate the complicated physical/electrochemical/chemical processes during the operation of PCFC running on ethane to achieve the cogeneration of ethylene and electricity. The model shows good agreement with the experimental data from the literature. The effects of operating voltage, inlet fuel flow rate, and inlet temperature on the PCFC electrochemical performance are well-investigated. Meanwhile, the effects of different operating conditions on ethylene production in PCFC are discussed in detail.

PCFC at 0.4 V outperforms PCFC under the OCV condition in terms of ethylene production due to the promotion of electrochemical reactions. At 700 °C, PCFC under OCV condition exhibits a C_2H_4 yield of 15.60 %, while PCFC reaches a C_2H_4 yield of 32.99 % and a PPD of 146.12mW cm^{-2}. As the operating voltage decreases, the increase in H_2 consumption results in higher current density and shifts the EDH process to the beneficial side. In addition, the cooling

31

area in the cell shrinks as the working voltage decreases. With the increase of inlet fuel flow rate, an optimum current density can be obtained, however, the yield of C_2H_4 keeps decreasing. As the inlet fuel flow increases, the temperature distribution is more uniform, while the cooling area expanded. Both current density and the yield of C_2H_4 are considerably improved with the increase in inlet temperature. It is worth noting that as the inlet temperature increases, the cooling area decreases while the temperature gradient increases. However, in the practical operation, the working temperature should be well-control to prevent the high temperature gradient and the generation of the by-product. Another interesting finding is the H_2 depletion in the anode layer is a critical bottleneck limiting the electrochemical performance of PCFC. The results show that up to 50 % of the electrochemically active area exhibits terrible local performance due to H_2 depletion. In future studies, it is necessary to develop a suitable operation strategy to increase the local H_2 concentration. In addition, inlet air flow rate has important implications for PCFC cogeneration performance since heat transfer and oxygen distribution can be affected by inlet air flow rate. Hence, in future studies, the impacts of inlet air flow rate on the cogeneration performance of PCFC will be quantitatively investigated and described. The structural and microstructural parameters, for instance, anode thickness and porosity, are capable to affect the PCFC performance. Due to the unclear effects of these parameters, future modelling efforts will strive to give a comprehensive description. The characteristics of cogeneration of electricity and ethylene in a C_2H_6-fueled PCFC are portrayed mathematically by this 2D model. It is favourable to incorporate ethylene production with electrical power generation in PCFC, which is a promising technology for replacing the current energy-/carbon-intensive thermal cracking process.

Acknowledgments

33

Reference

[1]   Chen J-M, Yu B, Wei Y-M. Energy technology roadmap for ethylene industry in China. Applied Energy 2018;224:160–74. https://doi.org/doi.org/10.1016/j.apenergy.2018.04.051.

[2]   Gao Y, Neal L, Ding D, Wu W, Baroi C, Gaffney AM, et al. Recent advances in intensified ethylene production—a review. ACS Catalysis 2019;9:8592–621. https://doi.org/doi.org/10.1021/acscatal.9b02922.

[3]   Zhao Z, Chong K, Jiang J, Wilson K, Zhang X, Wang F. Low-carbon roadmap of chemical production: A case study of ethylene in China. Renewable and Sustainable Energy Reviews 2018;97:580–91. https://doi.org/doi.org/10.1016/j.rser.2018.08.008.

[4]   Fairuzov D, Gerzeliev I, Maximov A, Naranov E. Catalytic dehydrogenation of ethane: A mini review of recent advances and perspective of chemical looping technology. Catalysts 2021;11:833. https://doi.org/doi.org/10.3390/catal11070833.

[5]   Saito H, Sekine Y. Catalytic conversion of ethane to valuable products through non-oxidative dehydrogenation and dehydroaromatization. RSC Advances 2020;10:21427–53. https://doi.org/oi.org/10.1039/D0RA03365K.

[6]   Gerzeliev Im, Fairuzov DK, Gerzelieva ZI, Maksimov Al. Production of Ethylene from Ethane Fraction by a Method Alternative to Steam Cracking. Russian Journal of Applied Chemistry 2019;92:1549–57. https://doi.org/doi.org/10.1134/S1070427219110120.

[7]   Bello IT, Zhai S, Zhao S, Li Z, Yu N, Ni M. Scientometric review of proton-conducting solid oxide fuel cells. International Journal of Hydrogen Energy 2021. https://doi.org/10.1016/j.ijhydene.2021.09.061.

[8]   Yu J, Ran R, Zhong Y, Zhou W, Ni M, Shao Z. Advances in porous perovskites:

34

synthesis and electrocatalytic performance in fuel cells and metal-air batteries. Energy & Environmental Materials 2020;3:121–45. https://doi.org/10.1002/eem2.12064.

[9]   Wang S, Luo J-L, Sanger AR, Chuang KT. Performance of ethane/oxygen fuel cells using yttrium-doped barium cerate as electrolyte at intermediate temperatures. The Journal of Physical Chemistry C 2007;111:5069–74. https://doi.org/doi.org/10.1021/jp066690w.

[10]   Garagounis I, Kyriakou V, Anagnostou C, Bourganis V, Papachristou I, Stoukides M. Solid electrolytes: applications in heterogeneous catalysis and chemical cogeneration. Industrial \& Engineering Chemistry Research 2011;50:431–72. https://doi.org/doi.org/10.1021/ie1001058.

[11]   Lin J-Y, Shao L, Si F-Z, Liu S-B, Fu X-Z, Luo J-L. Co2CrO4 nanopowders as an anode catalyst for simultaneous conversion of ethane to ethylene and power in proton-conducting fuel cell reactors. The Journal of Physical Chemistry C 2018;122:4165–71. https://doi.org/doi.org/10.1021/acs.jpcc.7b11680.

[12]   Liu S, Liu Q, Fu X-Z, Luo J-L. Cogeneration of ethylene and energy in protonic fuel cell with an efficient and stable anode anchored with in-situ exsolved functional metal nanoparticles. Applied Catalysis B: Environmental 2018;220:283–9. https://doi.org/doi.org/10.1016/j.apcatb.2017.08.051.

[13]   Li J, Hou J, Xi X, Lu Y, Li M, Fan Y, et al. Cogeneration of ethylene and electricity in symmetrical protonic solid oxide fuel cells based on a La0.6Sr0.4Fe0.8Nb0.1Cu0.1O3-δ electrode. Journal of Materials Chemistry A 2020;8:25978–85. https://doi.org/doi.org/10.1039/D0TA08974E.

[14]   Fan Y, Xi X, Li J, Wang Q, Li M-M, Wang L-J, et al. In-situ exsolved FeNi nanoparticles

35

on perovskite matrix anode for co-production of ethylene and power from ethane in proton conducting fuel cells. Electrochimica Acta 2021;393:139096. https://doi.org/doi.org/10.1016/j.electacta.2021.139096.

[15]   Ni M, Leung MKH, Leung DYC. Mathematical modeling of the coupled transport and electrochemical reactions in solid oxide steam electrolyzer for hydrogen production. Electrochimica Acta 2007;52:6707–18. https://doi.org/10.1016/j.electacta.2007.04.084.

[16]   Li Z, Zhang H, Xu H, Xuan J. Advancing the multiscale understanding on solid oxide electrolysis cells via modelling approaches: A review. Renewable and Sustainable Energy Reviews 2021;141:110863. https://doi.org/10.1016/j.rser.2021.110863.

[17]   Celik AN. Three-dimensional multiphysics model of a planar solid oxide fuel cell using computational fluid dynamics approach. International Journal of Hydrogen Energy 2018;43:19730–48. https://doi.org/10.1016/j.ijhydene.2018.08.212.

[18]   Wang Y, Zu B, Zhan R, Du Q, Ni M, Jiao K. Three-dimensional Modeling and Performance Optimization of Proton Conducting Solid Oxide Electrolysis Cell. Fuel Cells 2020;20:701–11. https://doi.org/https://doi.org/10.1002/fuce.201900246.

[19]   Yang X, Wei T, Chi B, Pu J, Li J. Lanthanum manganite-based perovskite as a catalyst for co-production of ethylene and hydrogen by ethane dehydrogenation. Journal of Catalysis 2019;377:629–37. https://doi.org/doi.org/10.1016/j.jcat.2019.08.008.

[20]   Galvita V, Siddiqi G, Sun P, Bell AT. Ethane dehydrogenation on Pt/Mg (Al) O and PtSn/Mg (Al) O catalysts. Journal of Catalysis 2010;271:209–19. https://doi.org/doi.org/10.1016/j.jcat.2010.01.016.

[21]   Sundaram KM, Froment GF. Modeling of thermal cracking kinetics—I: Thermal cracking of ethane, propane and their mixtures. Chemical Engineering Science

1977;32:601–8. https://doi.org/doi.org/10.1016/0009-2509(77)80225-X.

[22] Yancheshmeh MSS, Haghighi SS, Gholipour MR, Dehghani O, Rahimpour MR, Raeissi S. Modeling of ethane pyrolysis process: A study on effects of steam and carbon dioxide on ethylene and hydrogen productions. Chemical Engineering Journal 2013;215:550–60. https://doi.org/doi.org/10.1016/j.cej.2012.10.078.

[23] Szegner J, Yeung KL, Varma A. Effect of catalyst distribution in a membrane reactor: experiments and model. AIChE Journal 1997;43:2059–72. https://doi.org/doi.org/10.1002/aic.690430814.

[24] Wong KS, Thybaut JW, Tangstad E, Stöcker MW, Marin GB. Methane aromatisation based upon elementary steps: Kinetic and catalyst descriptors. Microporous and Mesoporous Materials 2012;164:302–12. https://doi.org/doi.org/10.1016/j.micromeso.2012.07.002.

[25] Dangwal S, Liu R, Kim S-J. High-temperature ethane dehydrogenation in microporous zeolite membrane reactor: Effect of operating conditions. Chemical Engineering Journal 2017;328:862–72. https://doi.org/doi.org/10.1016/j.cej.2017.07.108.

[26] Kong W, Li J, Liu S, Lin Z. The influence of interconnect ribs on the performance of planar solid oxide fuel cell and formulae for optimal rib sizes. Journal of Power Sources 2012;204:106–15. https://doi.org/10.1016/j.jpowsour.2012.01.041.

[27] Xu Q, Xia L, He Q, Guo Z, Ni M. Thermo-electrochemical modelling of high temperature methanol-fuelled solid oxide fuel cells. Applied Energy 2021;291:116832. https://doi.org/10.1016/j.apenergy.2021.116832.

[28] Błesznowski M, Sikora M, Kupecki J, Makowski Ł, Orciuch W. Mathematical approaches to modelling the mass transfer process in solid oxide fuel cell anode. Energy

2022;239:121878. https://doi.org/doi.org/10.1016/j.energy.2021.121878.

[29]   Kong W, Zhu H, Fei Z, Lin Z. A modified dusty gas model in the form of a Fick's model for the prediction of multicomponent mass transport in a solid oxide fuel cell anode. Journal of Power Sources 2012;206:171–8. https://doi.org/10.1016/j.jpowsour.2012.01.107.

[30]   Jiang Y, Virkar A V. Fuel composition and diluent effect on gas transport and performance of anode-supported SOFCs. Journal of the Electrochemical Society 2003;150:A942. https://doi.org/doi.org/10.1149/1.1579480.

[31]   Poling BE, Prausnitz JM, O'connell JP, others. The properties of gases and liquids. vol. 5. Mcgraw-hill New York; 2001.

[32]   Brokaw RS. Predicting transport properties of dilute gases. Industrial & Engineering Chemistry Process Design and Development 1969;8:240–53. https://doi.org/doi.org/10.1021/i260030a015.

[33]   Wilke CR, Chang P. Correlation of diffusion coefficients in dilute solutions. AIChE Journal 1955;1:264–70. https://doi.org/doi.org/10.1002/aic.690010222.

[34]   Neufeld PD, Janzen AR, Aziz R. Empirical equations to calculate 16 of the transport collision integrals $\Omega(l, s)^*$ for the Lennard-Jones (12-6) potential. The Journal of Chemical Physics 1972;57:1100–2. https://doi.org/doi.org/10.1063/1.1678363.

[35]   Andersson M, Paradis H, Yuan J, Sundén B. Three dimensional modeling of an solid oxide fuel cell coupling charge transfer phenomena with transport processes and heat generation. Electrochimica Acta 2013;109:881–93. https://doi.org/10.1016/j.electacta.2013.08.018.

[36]   Li Z, He Q, Xia L, Xu Q, Cheng C, Wang J, et al. Effects of cathode thickness and

microstructural properties on the performance of protonic ceramic fuel cell (PCFC): A 3D modelling study. International Journal of Hydrogen Energy 2021. https://doi.org/doi.org/10.1016/j.ijhydene.2021.11.022.

[37]   Su S, Zhang Q, Gao X, Periasamy V, Kong W. Effects of changes in solid oxide fuel cell electrode thickness on ohmic and concentration polarizations. International Journal of Hydrogen Energy 2016;41:16181–90. https://doi.org/10.1016/j.ijhydene.2016.04.221.

[38]   Chen B, Xu H, Sun Q, Zhang H, Tan P, Cai W, et al. Syngas/power cogeneration from proton conducting solid oxide fuel cells assisted by dry methane reforming: A thermal-electrochemical modelling study. Energy Conversion and Management 2018;167:37–44. https://doi.org/10.1016/j.enconman.2018.04.078.

[39]   Wang Q, Li L, Wang C. Numerical study of thermoelectric characteristics of a planar solid oxide fuel cell with direct internal reforming of methane. Journal of Power Sources 2009;186:399–407. https://doi.org/doi.org/10.1016/j.jpowsour.2008.10.034.

[40]   Xu H, Chen B, Zhang H, Sun Q, Yang G, Ni M. Modeling of direct carbon solid oxide fuel cells with H2O and CO2 as gasification agents. International Journal of Hydrogen Energy 2017;42:15641–51. https://doi.org/10.1016/j.ijhydene.2017.05.075.

[41]   Cai Q, Adjiman CS, Brandon NP. Investigation of the active thickness of solid oxide fuel cell electrodes using a 3D microstructure model. Electrochimica Acta 2011;56:10809–19. https://doi.org/10.1016/j.electacta.2011.06.105.